Food Chemistry 190 (2016) 142–149

Contents lists available at ScienceDirect

Food Chemistry

journal homepage: www.elsevier.com/locate/foodchem

Analytical Methods

Feasibility of combining spectra with texture data of multispectral imaging to predict heme and non-heme iron contents in pork sausages

Fei Ma [a], Hao Qin [a], Kefu Shi [a], Cunliu Zhou [a], Conggui Chen [a], Xiaohua Hu [c], Lei Zheng [a,b,*]

[a] School of Biotechnology and Food Engineering, Hefei University of Technology, Hefei 230009, Anhui Province, China
[b] School of Medical Engineering, Hefei University of Technology, Hefei 230009, Anhui Province, China
[c] School of Computer and Information, Hefei University of Technology, Hefei 230009, Anhui Province, China

ARTICLE INFO

Article history:
Received 28 January 2015
Received in revised form 14 May 2015
Accepted 18 May 2015
Available online 19 May 2015

Keywords:
Multispectral imaging
Heme iron
Non-heme iron
Pork sausage
Texture
Visualization

ABSTRACT

To precisely determine heme and non-heme iron contents in meat product, the feasibility of combining spectral with texture features extracted from multispectral imaging data (405–970 nm) was assessed. In our study, spectra and textures of 120 pork sausages (PSs) treated by different temperatures (30–80 °C) were analyzed using different calibration models including partial least squares regression (PLSR) and LIB support vector machine (Lib-SVM) for predicting heme and non-heme iron contents in PSs. Based on a combination of spectral and textural features, optimized PLSR models were obtained with determination coefficient (R^2) of 0.912 for heme and of 0.901 for non-heme iron prediction, which demonstrated the superiority of combining spectra with texture data. Results of satisfactory determination and visualization of heme and non-heme iron contents indicated that multispectral imaging could serve as a feasible approach for online industrial applications in the future.

© 2015 Elsevier Ltd. All rights reserved.

1. Introduction

Iron is a trace element of considerable concern in public health, and intake of iron is mainly by food-based approaches. Heme and non-heme iron are present in food as two forms of dietary iron (Carpenter & Clark, 1995; Carpenter & Mahoney, 1992; Turhan, Altunkaynak, & Yazici, 2004), and the former is of higher bioavailability, ranging from 15% to 35%, than the latter between 2% and 20% (Kalpalathika, Clark, & Mahoney, 1991). Meat is the main source of heme iron in human diets, and meanwhile, meat also makes great contribution to the non-heme iron content of human diets (Carpenter & Mahoney, 1992). Regular intake of meat can effectively prevent the occurrence of iron deficiency disorders which are affecting large fractions of the population, particularly menstruating and pregnant women (Kristensen & Purslow, 2001; Schönfeldt & Hall, 2011). However, a high-meat and low-fiber diet, more common in developed countries, has been associated with an increased risk of chronic diseases such as cancers, hypertension, coronary disease, and type 2 diabetes and the happening of these diseases may be related to the heme iron intake (Genkinger, Friberg, Goldbohm, & Wolk, 2012; Jessie, Celia, Alison, & Michael, 2009; Lajous et al., 2014; White & Collinson, 2013). Additionally, either heme or non-heme iron can act as a catalyst to accelerate lipid oxidation, which thus decreases the quality of meat and meat products (Kılıç, Şimşek, Claus, & Atılgan, 2014; Min, Cordray, & Ahn, 2010). In order to keep the nutritional values and quality standards as close as possible to the preference of the target consumer, the levels of heme and non-heme iron are often detected in meat and meat products. At present, the two most widely used methods for determination of heme and non-heme iron contents are the Hornsey method (Carpenter & Clark, 1995; Hornsey, 1956; Turhan et al., 2004) and Ferrozine method (Ahn, Wolfe, & Sim, 1993; Kristensen & Purslow, 2001; Li, Li, Xu, & Zhou, 2012), which are both time-consuming, laborious, and destructive and not suitable for analyzing large sums of samples. It would be very difficult to monitor real-time change of heme and non-heme iron contents during meat processing and storage. Therefore, developing a rapid and accurate method to evaluate heme and non-heme iron contents is vital for the meat product industry.

Multispectral imaging (MSI) is an emerging technology that integrates both spectroscopy and imaging in a single system, enabling acquisition of spatial and spectral information simultaneously from an object. A three-dimensional (3D) image (*hypercube*) captured by MSI system is consist of few feature-related

Abbreviations: MSI, multispectral imaging; PS, pork sausage; PSs, pork sausages; PLSR, partial least squares regression; Lib-SVM, Lib support vector machine; ROI, region of interest; R^2, coefficient of determination; SE, standard error; SEC, standard error of calibration; SEP, standard error of prediction; SPA, successive projections algorithm.

* Corresponding author at: School of Biotechnology and Food Engineering, Hefei University of Technology, Hefei 230009, Anhui Province, China.
E-mail addresses: lei.zheng@aliyun.com, lzheng@hfut.edu.cn (L. Zheng).

http://dx.doi.org/10.1016/j.foodchem.2015.05.084
0308-8146/© 2015 Elsevier Ltd. All rights reserved.

single-band images and each band of them was often selected from a large number of hyperspectral imaging researches in agri-food (Feng & Sun, 2012; Park, Lawrence, Windham, & Smith, 2006). The 3D data containing a large amount of information could be used to analyze and ascertain minor and/or subtle physical and chemical features in samples. Compared with hyperspectral imaging, less processing time make MSI easer to meet the speed requirement of industrial production lines used for online high-throughput screening to assess meat quality, nutrition, safety, and authenticity. In recent years, MSI technology as a rapid and nondestructive analysis method has been wildly applied in fishes (Dissing, Nielsen, Ersbøll, & Frosch, 2011), meats (Ma et al., 2014a; Ropodi, Pavlidis, Mohareb, Panagou, & Nychas, 2015), fruits (Lunadei, Galleguillos, Diezma, Lleó, & Ruiz-Garcia, 2011), vegetables (Løkke, Seefeldt, Skov, & Edelenbos, 2013), etc. However, almost all of these studies only utilized spectral data without incorporating information on spatial data, which has been successfully used to improve the accuracy of model prediction in hyperspectral imaging studies (He, Wu, & Sun, 2014; Pu, Sun, Ma, & Cheng, 2015). To the best of our knowledge, the use of multispectral image analysis for heme and non-heme iron contents in pork sausages (PSs) based on combination of spectral and textural features has never been previously explored.

The object of this research was to make a combination of spectral and spatial information to improve prediction accuracy of heme and non-heme iron contents in PSs. The specific objects of the study were to (1) extract spectral data from region of interest (ROI) after segmenting multispectral image of pork sausage (PS) acquired in the range of 405–970 nm; (2) extract texture feature variables from the first principal component image (accounted for 98.89% of the total variance) using gray level co-occurrence matrix (GLCM); (3) identify the important bands from the whole spectra (19 bands) using successive projection algorithm (SPA); (4) build partial least-squares regression (PLSR) and LIB support vector machine (Lib-SVM) models used for predicting heme and non-heme iron contents based on spectral and textural data; (5) visualize the distribution of heme and non-heme iron contents in PSs.

2. Materials and methods

2.1. Chemicals

Ferrozine [3-(2-pyridyl)-5,6-diphenyl-1,2,4-triazine-4′,4″-disulfonic acid sodium salt], neocuproine [2,9-dimethyl-1,10-phenanthroline] and hematin porcine were provided by Sigma–Aldrich Co., USA. Ascorbic acid (⩾99.7%) and $FeCl_2{\cdot}4H_2O$ (⩾99.8%) were purchased from Sinopharm Chemical Reagent Co., Ltd., China. All other reagents used were of analytical grade, and double deionized water was used throughout.

2.2. Reagents

Iron standard stock solution (100 μg Fe/mL) was prepared by dissolving 0.356 g $FeCl_2{\cdot}4H_2O$ in 1 L of 0.1 M HCl solution. Ferrozine color reagent was prepared by mixing 75 mg ferrozine and 75 mg neucoproine in 25 mL water containing 1 mL concentrated HCl and then stored at 4 °C. Ascorbic acid solution and acidified acetone were prepared within 24 h before use and respectively stored at 4 °C and 25 °C.

2.3. Sample preparation

Pork (hind leg) used for this work was purchased from a local supermarket of the Carrefour Group, and preparation were commenced within 30 min after purchase. After the visible fat and connective tissue were trimmed off, the pork was ground twice with a meat grinder (Shangyuan, SYP-MM 12, Guangdong Province, China) fitted with a plate of 6 mm diameter holes, vacuum packaged and stored at −20 °C. The ground pork was thawed overnight (about 12 h) at 4 °C before use every time and all thaw drip was retained. 1.5% salt (NaCl, w/w) was added into the ground pork and stirred fully to form a mixture, and then stored for 12 h at 4 °C. The final mixture was stuffed into Nylon/PE multilayer casing (19 mm in diameter) without entrapped air and sealed for further experiments.

In order to develop satisfactory prediction models for heme and non-heme iron contents, the prepared pork samples (ca. 20 g for each) were heated for 2 h in a water bath at different temperatures (30, 40, 50, 60, 70, and 80 °C), followed immediately by cooling in ice-water for about 30 min. These heated samples, namely PSs, were stored overnight at 4 °C and determinations were carried out the next day. Each PS was applied to analyze heme and non-heme iron contents simultaneously. All experiments used for analysis were repeated eight times, also known as eight batches. Eighty-four (84) PSs from six independent batches (14 PSs per batch) were used to establish the calibration models, and 36 PSs from the rest two batches were employed for the purpose of external validation. It should be noted that 120 PSs from six different temperatures (20 PSs at each temperature) were analyzed in total.

2.4. Iron determination

Heme iron method. Heme iron was determined using a modified procedure originally reported by Hornsey (1956) and Kristensen and Purslow (2001). In order to ensure that the concentration of acetone and HCl was respectively 80% and 2% in the final suspension, the moisture content of each PS should be firstly analyzed by oven drying method (Chinese National Standard 5009.3-2010, 2010). Subsequently, the acidified acetone was prepared based on the moisture content of the PS. Five grams of PS was placed in a 50 mL pol-propylene centrifuge tube and 10 mL of acidified acetone was added. The mixture was then homogenized for 15 s at 15, 000 rpm using a high-speed dispersator (XHF-D, Ningbo Scientz Biotechnology Co., Ltd., China) with a stainless steel dispersing element, which was rinsed twice with acidified acetone solution before use. Afterwards, the dispersing element was immediately rinsed 3 times with 3 mL of acidified acetone and these suspensions were briefly mixed and stored at 4 °C in the dark for 1 h. Then, the insoluble substances were precipitated by high-speed centrifugation for 10 min at 10, 000 × g (4 °C) using a CT14RD freezing centrifuge (Techcomp Co., Ltd., Shanghai) and the clear supernatant was filtered through a glass microfiber filter (GF/A, Whatman, Maidstone, England). The absorbance of the filtrate at 640 nm was measured by a Spectral Scanning Multimode Reader (Varioskan Flash, Thermo Fisher Scientific Inc., USA). The heme iron concentration in the PS was calculated from the standard curve that was established by plotting the absorbance against the several concentrations of Hematin (0, 5, 10, 20, 40, 60, and 80 ppm) in acidified acetone solution (80% acetone and 2% HCl). The represented equation of $y_{(\text{Hematin})} = 10692x_{(\text{Absorbance})} - 0.2074$ was obtained with determination coefficient (R^2) of 0.997. Finally, the heme iron content in hematin was calculated as follow:

$$\text{Heme iron (ppm)} = \text{Hematin content (ppm)} \times \text{AW/MW} \quad (1)$$

where AW and MW were the atomic weight of iron and the molecular weight of hematin, respectively.

Non-heme method. Non-heme iron was analyzed by the Ferrozine method described by Kristensen and Purslow (2001) and Ahn et al. (1993) with a slight modification. Five grams of PS was transferred to a 50 mL poly-propylene centrifuge tube and

15 mL citrate–phosphate buffer (0.1 M, pH 5.5) was added. The suspension was homogenized for 15 s at 15, 000 rpm using the XHF-D dispersator, the dispersing element of which was rinsed twice with citrate–phosphate buffer before use. A 3 mL of homogenate was mixed with 1 mL of 2% ascorbic acid in 0.2 M HCl and incubated at room temperature (20 °C) for 20 min. Then, 2 mL of 11.3% trichloroacetic acid was added and mixed thoroughly, followed by high-speed centrifugation for 10 min at 10,000×*g* (10 °C) using the CT14RD centrifuge. Three milliliters of the clear supernatant was transferred to a 10 mL centrifuge tube, mixed fully with 1.2 mL of 10% ammonium acetate and 0.3 mL of ferrozine color reagent. The mixture was filtered through a GF/A Whatman filter paper and the absorbance was measured at 562 nm by the Varioskan Flash Spectral Reader. The concentration of non-heme iron was calculated by regression equation of $y_{(\text{Non-heme iron})} = 16.045x_{(\text{Absorbance})} - 0.6241$ ($R^2 = 0.999$), which was provided by plotting the absorbance against the several concentrations of iron standard solutions (0, 1, 2, 3, 4, 5, and 6 ppm).

All the steps for iron determination should be carried out in dark or under very dim light illumination.

2.5. Image acquisition and analysis

Image acquisition. Images from PSs were captured using VideometerLab equipment (Videometer A/S, Hørsholm, Denmark), which acquires multispectral images in 19-non-uniformly distributed-different wavelengths ranging from 405 to 970 nm and the detailed band values of the measured wavelengths were 405, 435, 450, 470, 505, 525, 570, 590, 630, 645, 660, 700, 780, 850, 870, 890, 910, 940, and 970 nm. A detailed description of the instrument (shown in Fig. 1) has been reported in previous study (Ma et al., 2014b). The system should be preheated at least 30 min before image acquisition and subsequently calibrated using one uniform bright, one uniform dark and one geometric disc which is white a grid of black dots. Multispectral images of PSs were acquired, recorded, and stored in a form of 3D '*hypercube*' ($2056 \times 2056 \times 19$) containing both spectral (19) and spatial (2056×2056) information.

Spectral extraction. Prior to extracting spectrum, the ROI was firstly identified based on image segmentation process, which can be easily finished due to the distinctive spectral differences between PS and background spectrum. Based on a simple threshold at value of 0.2, a segmented image of the PS has been produced. Thus, the multispectral image of PS without the background materials, namely ROI, could be transformed to spectrum by mean calculation.

Texture extraction. As one of the most important image features, texture represent the spatial arrangement of the gray levels of the pixels within the ROI (He et al., 2014). First, principal component analysis (PCA) was applied to select the first three principal component (PC) images (shown in Fig. 1) that captured the majority of the variance, where PC1, PC2, and PC3 explained 98.89%, 0.22%, and 0.08% of variance, respectively. In this study, the first PC score image was selected to extract texture data using Gray level co-occurrence matrix (GLCM) analysis method that could provide a number of second-order statistics used to describe the gray level relationships within a neighborhood around a pixel of interest (Kruizinga & Petkov, 1999). A total of 5 s-order statistical textural variables were extracted, including energy, correlation, entropy, contrast, and homogeneity. For the first PC score image, five distances from 1 to 5 pixels and four directions (0°, 45°, 90°, and 135°) were implemented to extract textural features and then these textural values were averaged into one value that represent the textural feature of the PS. The textural feature values were obtained by calculation of five equations (Eqs. (2)–(6)).

$$\text{Energy} = \sum_{i,j}[M_{D,\theta}(i,\ j)]^2 \tag{2}$$

$$\text{Correlation} = \frac{\sum_{i,j}(ij)M_{D,\theta}(i,\ j) - u_i u_j}{\sigma_i \sigma_j} \tag{3}$$

$$\text{Entropy} = -\sum_{i,j} M_{D,\theta}(i,\ j)\log M_{D,\theta}(i,\ j) \tag{4}$$

$$\text{Contrast} = \sum_{i,j}(i-j)^2 M_{D,\theta}(i,\ j) \tag{5}$$

$$\text{Homogeneity} = \sum_{i,j}\frac{M_{D,\theta}(i,\ j)}{1+(i+j)^2} \tag{6}$$

where (i, j) is the coordination of the pixel of interest, D is the given distance between two pixels, θ is the offset direction of the pair of pixels over an image (0°, 45°, 90°, and 135°), $M_{D,\theta}$ is the obtained GLCM matrix, $M_{D,\theta}$ (i, j) is the value in element $\{i, j\}$ of $M_{D,\theta}$, μ_i and μ_j are the means of $M_{D,\theta}$ (i, j) in the row and column directions, and σ_i and σ_j are the standard deviations of $M_{D,\theta}$ (i, j) in the row and column directions.

2.6. Data analysis

In this work, the methods of SPA, PLSR, and Lib-SVM were applied to analyze the experiment data including whole wavelengths, important wavelengths, and textures features and their main steps were shown in Fig. 1. Details of analytical methods were introduced below.

PLSR is a classic multivariate data analysis method which decomposes both *X* and *Y* features, extracts the latent factors, and searches the optimal functions by minimizing the error sum squares. It is particularly suit to analyze data with strongly collinear, noisy, and numerous variables in the predictor matrix *X* (i.e. independent variables) and responses *Y* (i.e. dependent variables) (Panagou, Mohareb, Argyri, Bessant, & Nychas, 2011). The robustness of calibration models used for this work was tested by using split cross validation.

Lib-SVM is an optimized version based on the standard SVM that is powerful for solving problems in nonlinear classification, function estimation, and density estimation. For the user not familiar with *Machine Learning Methods*, it is considered easier to use than *Neural Networks*. SVM transform a complex space formed by nonlinear mapping of multivariate input vector into a higher dimensional linear space through the use of a kernel function. To obtain good performances, *c* and *g* as two key kernel parameters in Lib-SVM model should be optimized by a 5-fold inner cross validation process. Lib-SVM was performed according to the method of Chang and Lin (2011).

SPA is a novel variable algorithm designed to select subsets of variables with minimum of collinearity by simple projection operations in a vector space (Ye, Wang, & Min, 2008). The principle of variable selection by SPA is that candidate subsets of variables are constructed based on the maximum projection value on the orthogonal subspace of the previous variable. In order to further simply the computation and accelerate the data processing, SPA was implemented for removing a lot of redundancy or irrelevant information that was contained in '*hypercube*'. Thus, the important spectral bands were selected to develop new calibration models.

A total of 84 PSs with different temperature treatment (30–80 °C) were applied to establish calibration models, and the accuracy and robustness of these models were evaluated by an external validation set (36 PSs) that was obtained independently. The

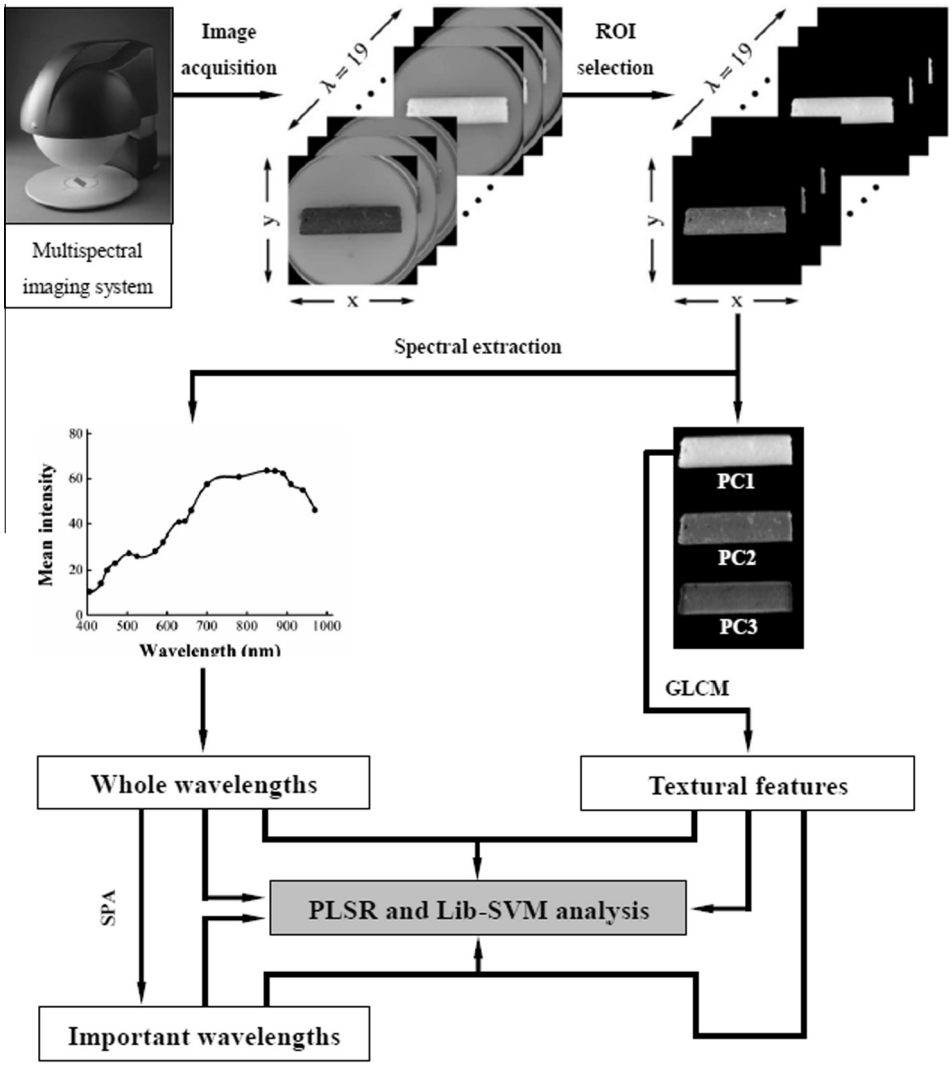


Fig. 1. Flow chart of main steps in data acquisition and analysis for predicting heme and non-heme iron contents of PSs.

predict ability of these models was evaluated in terms of R^2 of measured values versus predicted values, standard error of calibration (SEC), standard error of prediction (SEP), and the ratio of performance to deviation (RPD). It is always expected to obtain a high R^2, a high RPD, and a low standard error (SE). SEC, SEP, and RPD were defined as the following equations (Eqs. (7)–(11)):

$$\mathrm{SEC} = \sqrt{\frac{1}{I_C - 1}\sum_{i=1}^{I_C}(\hat{y}_i - y_i)^2} \tag{7}$$

$$\mathrm{bias} = \frac{1}{I_P}\sum_{i=1}^{I_P}(\hat{y}_i - y_i) \tag{8}$$

$$\mathrm{SEP} = \sqrt{\frac{1}{I_P - 1}\sum_{i=1}^{I_P}(\hat{y}_i - y_i - \mathrm{bias})^2} \tag{9}$$

$$\mathrm{SD} = \sqrt{\frac{1}{n - 1}\sum_{i=1}^{n}(y_i - \bar{y})^2} \tag{10}$$

$$\mathrm{RPD} = \frac{\mathrm{SD}}{\mathrm{SEP}} \tag{11}$$

where $\hat{y}_i$ is predicted value in sample number i, y_i is measured value in sample number i, I_C is the number of samples in the calibration set (84), I_P is the number of samples in the prediction set (36), and $\bar{y}$ is the measured average value in sample number n. *bias* and standard deviation (*SD*) as two intermediate variables were used to calculate SEP and RPD, respectively.

2.7. Visualization

Besides obtaining the quantitative relationship between spectral and physicochemical attributes of PS like spectroscopic technique, MSI can visualize the distribution of the physicochemical attributes within each PS according to its imaging ability. Spectral data of heme and non-heme iron of each pixel would be required to establish accurate prediction models accordingly. However, it is impossible to detect any one of the two iron contents of a pixel. To solve this problem, the best and simplest linear model for each kind of iron that was constructed based on mean spectrum at selected important wavelengths. First, the linear model was transferred to the spectrum of each pixel for predicting the iron content accordingly. The spatial position of each pixel along with its iron content was then used to form the distribution map of iron within PS. The detailed steps involved in visualization were depicted in previous study (Ma et al., 2014a).

2.8. Software

Image segmentation and spectrum extraction were finished by using VideometerLab software version 2.10 (Videometer A/S, H, Denmark). PLSR analysis was programmed in SAS 9.1 (SAS Institute Inc., USA). Texture extraction, SPA, Lib-SVM, and visualization were carried out by writing a procedure in Matlab 7.11 (The Mathworks Inc., Natick, MA, USA).

3. Results and discussion

3.1. Heme and non-heme iron contents in PSs

The content of heme and non-heme iron in PSs was measured after processing with six different temperatures (30, 40, 50, 60, 70, and 80 °C) and the measured results were shown in Fig. 2. Compared with the lower cooking temperature (30–40 °C), the treatment of 50–80 °C significantly decreased the heme iron content of PSs and significantly increased non-heme iron content of that ($P < 0.05$). From 30 °C to 80 °C an interested phenomenon was that the decrease in heme iron content was followed by an increase in non-heme iron content of the PSs. The correlation coefficient (r) between the means of heme and non-heme iron detections at the six temperatures was −0.773, which indicated that the increase of non-heme iron content in PSs during cooking was likely transformed from heme iron. The inverse relationship between heme and non-heme iron contents caused by cooking temperature was in agreement with other studies (Carpenter & Clark, 1995; Kristensen & Purslow, 2001). The major part of heme iron in meat is located in myoglobin and the thermal denaturtion degree of myoglobin could not only change heme and non-heme iron contents in meat products (Hargrove & Olson, 1996; Kristensen & Purslow, 2001), but also affect some quality features such as color, flavor, and lipid oxidation (Faustman, Sun, Mancini, & Suman, 2010; Yancey et al., 2006). Based on these changes in quality attributes and chemical compositions, MSI technology has a potential to detect heme and non-heme iron contents in PSs.

3.2. Spectral profiles

Average spectra of PSs in various cooking temperatures were displayed in Fig. 3. It is characteristic that the reflectance of the PS increased in most wavelengths of the spectrum with increasing cooking temperatures, and the difference of these spectral features might be caused by changes of biochemical and textural

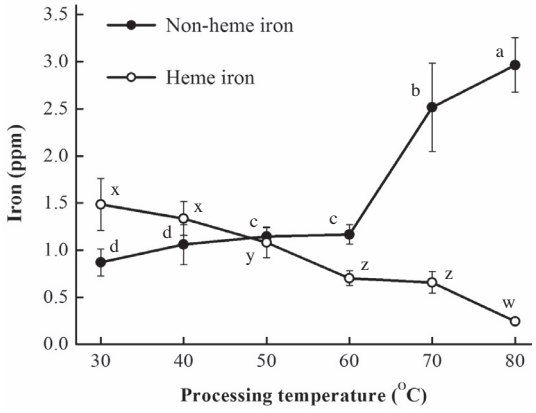


Fig. 2. The average value of heme and non-heme iron contents in PSs treated at different cooking temperatures (30–80 °C) for 2 h. Vertical bars represent standard deviations from twenty PSs, and each of them was repeated at least two times. The Pearson correlation coefficient (r) between heme and non-heme iron was −0.773.

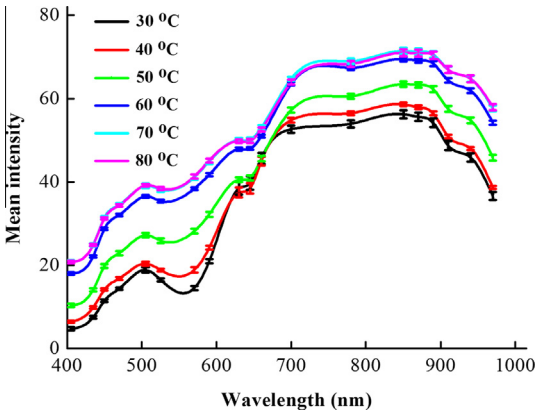


Fig. 3. Average spectra from the multispectral images of PSs treated at six cooking temperatures (30, 40, 50, 60, 70, and 80 °C). Vertical bars represent standard deviations from twenty PSs.

characteristics in PSs. As seen in Fig. 3, one major difference in spectral intensities was found in the range of 510–650 nm, which was associated with heme pigments like hemoglobin, myoglobin, etc. and their oxides such as methemoglobin and metmyoglobin (Liu et al., 2003; Sivertsen, Heia, Hindberg, & Godtliebsen, 2012). Additionally, the absorption spectra between 750 and 970 nm arose from combination of symmetric and antisymmetric O–H stretching and bending modes (Liu, Qu, Sun, Pu, & Zeng, 2013), which should make it easier to understand the major difference of absorption wavelengths ranging from 750 to 970 nm that related to moisture loss (reduce from 73.75% to 70.25%) caused by changing of cooking temperature (detailed data not shown). Therefore, these differences and changes provided a strong evidence for the effectiveness of MSI in detecting the heme and non-heme iron contents in PSs.

3.3. Prediction of heme and non-heme iron contents using spectra and textures

The selection of an optimum calibration method is greatly important in spectral analysis. The quantitative models used for predicting heme and non-heme iron contents were established by using PLSR and Lib-SVM analysis methods. The results of multivariate analysis based on spectral and textural features (extraction steps were detailed in the Section 2.5) were shown in Table 1. The Lib-SVM model established by whole spectra was accurate for predicting heme iron content in PSs with R_P^2 of 0.880 and RPD of 2.885. When PLSR was used to build the calibration model, compared to the result of Lib-SVM model, an improvement of 3.4% and 13.8% was obtained for R_P^2 and RPD, respectively. And likewise, the PLSR model was more accurate and robust than Lib-SVM model for the prediction of non-heme iron content in PSs. The R_P^2, SEP, and RPD were respectively 0.891, 0.298, and 2.981 for PLSR model that was also established by the whole spectral data. In order to further improve data acquisition and processing speed, two groups of important wavelengths selected by SPA were 405, 435, 450, 570, 590, 645, and 660 nm and 435, 470, 570, 590, 645, 780, and 870 nm, which were respectively applied to predict heme and non-heme iron contents in PSs. Although the accuracy of whatever PLSR or Lib-SVM model based on important bands was slightly reduced in heme and non-heme iron prediction (Table 1), the implementation of a few number of wavelength variables could reduce the time required for image acquisition. Thereby, these selected wavelengths could serve as a reference for industrial applications. Compared to those models established by whole and important spectral data, it was not hard to find that all those

Table 1
Calibration and prediction results for heme and non-heme iron contents in PSs treated at different cooking temperatures (30–80 °C) using MSI technique.[a]

Features	Calibration model	Variable number	Calibration		Prediction		
			R_C^2	SEC	R_P^2	SEP	RPD
Heme iron							
Whole spectra	PLSR	19	0.894	0.147	0.911	0.136	3.348
	Lib-SVM	19	0.893	0.148	0.880	0.158	2.885
Textures	PLSR	5	0.733	0.234	0.796	0.208	2.197
	Lib-SVM	5	0.807	0.199	0.759	0.225	2.028
Whole spectra–textures	PLSR	24	0.903	0.141	**0.912**	**0.136**	**3.356**
	Lib-SVM	24	0.928	0.122	0.878	0.161	2.843
Important spectra	SPA–PLSR	7	0.858	0.171	0.864	0.169	2.700
	SPA–Lib-SVM	7	0.847	0.177	0.864	0.169	2.705
Important spectra–textures	SPA–PLSR	12	0.862	0.168	0.859	0.171	2.669
	SPA–Lib-SVM	12	0.919	0.129	0.842	0.190	2.402
Non-heme iron							
Whole spectra	PLSR	19	0.920	0.235	0.891	0.298	2.981
	Lib-SVM	19	0.922	0.232	0.870	0.331	2.685
Textures	PLSR	5	0.578	0.538	0.560	0.592	1.502
	Lib-SVM	5	0.762	0.409	0.595	0.568	1.566
Whole spectra–textures	PLSR	24	0.936	0.210	**0.901**	**0.281**	**3.167**
	Lib-SVM	24	0.936	0.210	0.851	0.352	2.529
Important spectra	SPA–PLSR	7	0.913	0.245	0.867	0.324	2.741
	SPA–Lib-SVM	7	0.936	0.210	0.879	0.316	2.817
Important spectra–textures	SPA–PLSR	12	0.914	0.243	0.875	0.316	2.817
	SPA–Lib-SVM	12	0.934	0.215	0.826	0.378	2.352

[a] SEC: standard error of calibration; SEP: standard error of prediction; R^2: determination coefficient between the predicted and measured values; RPD: ratio of performance to deviation; Bold values highlight the best results in the data processing.

models using only image information (five textures) have lower performance in predicting heme and non-heme iron contents of PSs. This might be because the spectral data had greater contribution than the textural features in building the PLSR and Lib-SVM models. Furthermore, spectral information could explain the internal attributes (chemical compositions, tissue structure, etc.) and external attributes such as color in PSs, which were closely related to dietary iron changes, while textural changes occurred during the cooking process did not have significant relation with the dietary iron evolution, hence, the prediction results were not very satisfying (Table 1). To fully play the advantages of MSI technique, the spectral and image information should be combined to build more precise prediction models for heme and non-heme iron contents. Results showed that PLSR analysis method was more suitable for predicting heme and non-heme iron contents in PSs than Lib-SVM by combining spectral with texture features. Two largest RPD values for detecting heme and non-heme iron contents were respectively 3.356 and 3.167 (Table 1 and Fig. 4), which were considered adequate for analytical purposes (Nicolaï et al., 2007; Xiong, Sun, Zeng, & Xie, 2014). Concluded from above, it can be discovered that MSI as a rapid and accuracy method for analyzing dietary iron content in PSs has great value for storage, processing, and consumption of meat products.

3.4. Visualization

The implement of visualization process would be helpful to understand the variation of heme and non-heme iron contents in PSs during cooking, which is impossible to identify by naked eye. In this work, PLSR models established by whole spectra had good prediction accuracy with RPD of 3.348 for heme and of 2.981 for non-heme iron, though not as compact as the PLSR prediction models built by combined whole spectra with textures (Table 1), which were adequate for using to generate the heme and non-heme iron distribution maps of PSs.

As shown in Fig. 5, RGB images under a black background could be used to easily identify color changes caused by different cooking temperatures that had previously been associated with variation of

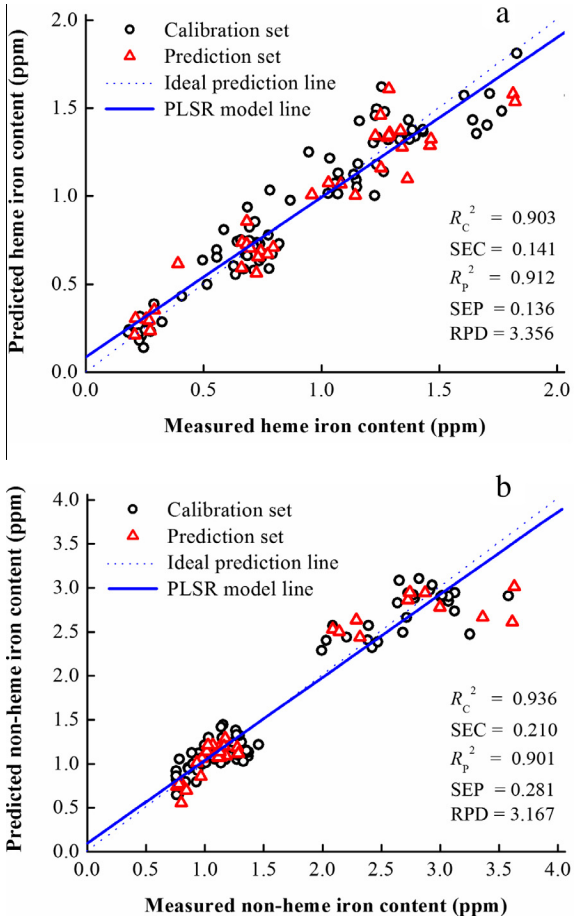


Fig. 4. Measured and predicted heme (a) and non-heme (b) iron contents in PSs for calibration set and prediction set by PLSR analysis based on a combination of whole spectra (405–970 nm) and textures (SEC: standard error of calibration; SEP: standard error of prediction; R^2: determination coefficient between the predicted and measured values; RPD: ratio of performance to deviation).

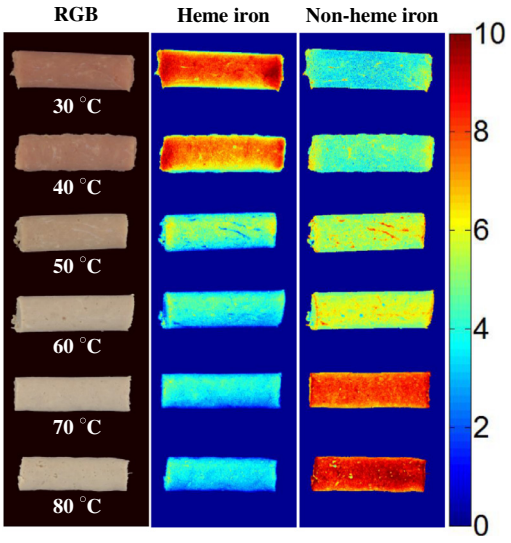


Fig. 5. Distribution maps of heme and non-heme iron contents in PSs. The vertical color bar represents the intensity values of the images. (For interpretation of the references to colour in this figure legend, the reader is referred to the web version of this article.)

heme and non-heme iron (Estévez & Cava, 2004; Li et al., 2012). However, the distribution of heme and non-heme iron contents in PSs were hard to detect with naked eyes by those RGB images. To achieve visualization, multispectral images of PSs were applied to calculate in pixels based on PLSR prediction models. Thus, the distribution images for heme and non-heme iron contents in PSs were visualized by mapping their values with a linear color scale where the different heme and non-heme iron contents from low to high were shown in different colors from blue to red (color bar at the right in Fig. 5). Different colors in the distribution maps implied different heme and non-heme iron contents within the PS in proportion to the spectral differences of pixels. The pixels with low heme and non-heme iron contents were shown in blue and green, while the pixels in orange and red are those with high heme and non-heme iron contents. With cooking temperature increasing (range from 30 °C to 80 °C), the change regularity of color pixels was in accord with the measurement results of heme and non-heme iron contents by comparing Figs. 2 with 5. These distribution maps offered a more intuitive and comprehensive assessment of heme and non-heme iron contents at each pixel in PSs, and also proved the importance and usefulness of MSI in evaluation of nutritional quality related to dietary iron in meat products.

4. Conclusions

The heme and non-heme iron, two main forms of dietary iron in sausages, could be rapidly and nondestructively detected by MSI technique in this work, which was greatly important to formulate a reasonable dietary intake program based on nutritional status of human body. Results showed that the combination of spectral and textural features was more effective than when the spectra or textures were used alone for evaluating heme and non-heme iron contents in PSs. Two best models used for predicting heme (R_P^2 = 0.912, RPD = 3.356) and non-heme iron (R_P^2 = 0.901, RPD = 3.167) contents were obtained by PLSR analysis based on combined whole spectra with five textures. Besides, the distribution of heme and non-heme iron contents in PSs could be visualized by image algorithm. The overall results suggested that MSI technology would be a good alternative to the time-consuming and destructive chemistry method for detecting dietary iron content in meat products, and hence would become a valuable direction for meat industry.

Acknowledgements

The authors would like to thank the helps of Miss Jing Yao, Dr. Changhong Liu, Miss Shanshan Shui, and Mr Qiu Wang in the experiments that mainly included pretreatment of raw meat, image analysis, and so on. This study is supported by the specialized Fund for the National Key Technologies R&D Programme (2012BAD07B01), the Doctoral Program of Higher Education (20120111110024), the Anhui Province Key Technologies Research & Development Program (1301031033), the Key Project of Anhui Provincial Educational Department (KJ2014ZD26), the Fundamental Research Funds for the Central Universities (2012HGCX0003), and the Funds for Huangshan Professorship of Hefei University of Technology (407-037019).

References

Ahn, D., Wolfe, F., & Sim, J. (1993). Three methods for determining nonheme iron in turkey meat. *Journal of Food Science, 58*(2), 288–291.
Carpenter, C. E., & Clark, E. (1995). Evaluation of methods used in meat iron analysis and iron content of raw and cooked meats. *Journal of Agriculture and Food Chemistry, 43*, 1824–1827.
Carpenter, C. E., & Mahoney, A. W. (1992). Contributions of heme and nonheme iron to human nutrition. *Critical Reviews in Food Science and Nutrition, 31*(4), 333–367.
Chang, C.-C., & Lin, C.-J. (2011). LIBSVM: A library for support vector machines. *ACM Transactions on Intelligent Systems and Technology (TIST), 2*(3), 27.
Chinese National Standard (5009.3-2010). (2010). Determination of moisture in foods, Chinese National Hygiene Ministry, Beijing.
Dissing, B. S., Nielsen, M. E., Ersbøll, B. K., & Frosch, S. (2011). Multispectral imaging for determination of astaxanthin concentration in salmonids. *PLoS ONE, 6*(5), e19032.
Estévez, M., & Cava, R. (2004). Lipid and protein oxidation, release of iron from heme molecule and colour deterioration during refrigerated storage of liver pâté. *Meat Science, 68*(4), 551–558.
Faustman, C., Sun, Q., Mancini, R., & Suman, S. P. (2010). Myoglobin and lipid oxidation interactions: Mechanistic bases and control. *Meat Science, 86*(1), 86–94.
Feng, Y.-Z., & Sun, D.-W. (2012). Application of hyperspectral imaging in food safety inspection and control, a review. *Critical Reviews Food Science and nutrition, 52*(11), 1039–1058.
Genkinger, J. M., Friberg, E., Goldbohm, R. A., & Wolk, A. (2012). Long-term dietary heme iron and red meat intake in relation to endometrial cancer risk. *American Journal of Clinical Nutrition, 96*(4), 848–854.
Hargrove, M. S., & Olson, J. S. (1996). The stability of holomyoglobin is determined by heme affinity. *Biochemistry, 35*, 11310–11318.
He, H.-J., Wu, D., & Sun, D.-W. (2014). Potential of hyperspectral imaging combined with chemometric analysis for assessing and visualising tenderness distribution in raw farmed salmon fillets. *Journal of Food Engineering, 126*, 156–164.
Hornsey, H. C. (1956). The colour of cooked cured pork. I.-Estimation of the Nitric oxide – Haem Pigments. *Journal of the Science of Food and Agriculture, 7*(8), 534–540.
Jessie, J. M. F. W., Celia, J. P., Alison, M. S., & Michael, E. J. W. (2009). Consumption of red or processed meat does not predict risk factors for coronary heat disease; results from a cohort of British adults in 1989 and 1999. *European Journal of Clinical Nutrition, 63*(3), 303–311.
Kalpalathika, P. V., Clark, E. M., & Mahoney, A. W. (1991). Heme iron content in selected ready-to-serve beef products. *Journal of Agriculture and Food Chemistry, 39*, 1091–1093.
Kılıç, B., Şimşek, A., Claus, J. R., & Atılgan, E. (2014). Encapsulated phosphates reduce lipid oxidation in both ground chicken and ground beef during raw and cooked meat storage with some influence on color, pH, and cooking loss. *Meat Science, 97*, 93–103.
Kristensen, L., & Purslow, P. P. (2001). The effect of processing temperature and addition of mono- and di-valent salts on the heme- nonheme-iron ratio in meat. *Food Chemistry, 73*, 433–439.
Kruizinga, P., & Petkov, N. (1999). Nonlinear operator for oriented texture. *IEEE Transactions on Image Process, 8*(10), 1395–1407.
Lajous, M., Bijon, A., Fagherazzi, G., Rossignol, E., Boutron-Ruault, M. C., & Clavel-Chapelon, F. (2014). Processed and unprocessed red meat consumption and hypertension in women. *American Journal of Clinical Nutrition, 100*(3), 948–952.
Li, H., Li, C. B., Xu, X. L., & Zhou, G. H. (2012). Effects of illumination and packaging on non-heme iron and color attributes of sliced ham. *Meat Science, 91*, 521–526.
Liu, Y., Lyon, B. G., Windham, W. R., Realini, C. E., Pringle, T. D. D., & Duckett, S. (2003). Prediction of color, texture, and sensory characteristics of beef steak by visible and near infrared reflectance spectroscopy. A feasibility study. *Meat Science, 65*(3), 1107–1115.

Liu, D., Qu, J., Sun, D.-W., Pu, H., & Zeng, X.-A. (2013). Non-destructive prediction of salt contents and water activity of porcine meat slices by hyperspectral imaging in a salting process. *Innovative Food Science and Emerging Technologies, 20*, 316–323.

Løkke, M. M., Seefeldt, H. F., Skov, T., & Edelenbos, M. (2013). Color and textural quality of packaged wild rocket measured by multispectral imaging. *Postharvest Biology and Technology, 75*, 86–95.

Lunadei, L., Galleguillos, P., Diezma, B., Lleó, L., & Ruiz-Garcia, L. (2011). A multispectral vision system to evaluate enzymatic browning in fresh-cut apple slices. *Postharvest Biology and Technology, 60*(3), 225–234.

Ma, F., Wang, J., Liu, C., Lu, X., Chen, W., Chen, C., et al. (2014a). Discrimination of kernel quality characteristics for sunflower seeds based on multispectral imaging approach. *Food Analytical Methods*. http://dx.doi.org/10.1007/s12161-014-0038-x.

Ma, F., Yao, J., Xie, T., Liu, C., Chen, W., Chen, C., et al. (2014b). Multispectral imaging for rapid and non-destructive determination of aerobic plate count (APC) in cooked pork sausages. *Food Research International, 62*, 902–908.

Min, B., Cordray, J. C., & Ahn, D. U. (2010). Effect of NaCl, myoglobin, Fe(II), and Fe(III) on lipid oxidation of raw and cooked chicken breast and beef loin. *Journal of Agriculture and Food Chemistry, 58*(1), 600–605.

Nicolaï, B. M., Beullens, K., Bobelyn, E., Peirs, A., Saeys, W., Theron, K. I., et al. (2007). Nondestructive measurement of fruit and vegetable quality by means of NIR spectroscopy: A review. *Postharvest Biology and Technology, 46*, 99–118.

Panagou, E. Z., Mohareb, F. R., Argyri, A. A., Bessant, C. M., & Nychas, G. J. E. (2011). A comparison of artificial neural networks and partial least squares modelling on Fourier transform infrared spectral fingerprints. *Food Microbiology, 28*(4), 782–790.

Park, B., Lawrence, K. C., Windham, W. R., & Smith, D. P. (2006). Performance of hyperspectral imaging system for poultry surface fecal contaminant detection. *Journal of Food Engineering, 75*, 340–348.

Pu, H., Sun, D.-W., Ma, J., & Cheng, J.-H. (2015). Classification of fresh and frozen-thawed pork muscles using visible and near infrared hyperspectral imaging and textural analysis. *Meat Science, 99*, 81–88.

Ropodi, A. I., Pavlidis, D. E., Mohareb, F., Panagou, E. Z., & Nychas, G.-J. E. (2015). Multispectral image analysis approach to detect adulteration of beef and pork in raw meats. *Food Research International, 67*, 12–18.

Schönfeldt, H. C., & Hall, N. G. (2011). Determining iron bio-availability with a constant heme iron value. *Journal of Food Composition and Analysis, 24*(4), 738–740.

Sivertsen, A. H., Heia, K., Hindberg, K., & Godtliebsen, F. (2012). Automatic nematode detection in cod fillets (*Gadus morhua* L.) by hyperspectral imaging. *Journal of Food Engineering, 111*(4), 675–681.

Turhan, S., Altunkaynak, T. B., & Yazici, F. (2004). A note on the total and heme iron contents of ready-to-eat doner kebabs. *Meat Science, 67*, 191–194.

White, D. L., & Collinson, A. (2013). Red meat, dietary heme iron, and risk of type 2 diabetes: The involvement of advanced lipoxidation end products. *Advances Nutrition, 4*, 403–411.

Xiong, Z., Sun, D.-W., Zeng, X.-A., & Xie, G. (2014). Recent developments of hyperspectral imaging systems and their applications in detecting quality attributes of red meats: A review. *Journal of Food Engineering, 132*, 1–13.

Yancey, E. J., Grobbel, J. P., Dikeman, M. E., Smith, J. S., Hachmeister, K. A., Chambers, E. C. IV,, et al. (2006). Effects of total iron, myoglobin, hemoglobin, and lipid oxidation of uncooked muscles on livery flavor development and volatiles of cooked beef steaks. *Meat Science, 73*(4), 680–686.

Ye, S., Wang, D., & Min, S. (2008). Successive projections algorithm combined with uninformative variable elimination for spectral variable selection. *Chemometrics and Intelligent Laboratory Systems, 91*(2), 194–199.